Journal of Membrane Science 531 (2017) 86–93

Contents lists available at ScienceDirect

Journal of Membrane Science

journal homepage: www.elsevier.com/locate/memsci

# ALD-seeded hydrothermally-grown Ag/ZnO nanorod PTFE membrane as efficient indoor air filter

Shasha Feng[a], Dongyan Li[b], Ze-xian Low[c], Zhongyun Liu[d], Zhaoxiang Zhong[a,*], Yunxia Hu[d], Yong Wang[a], Weihong Xing[a]

[a] State Key Laboratory of Materials-Oriented Chemical Engineering, National Engineering Research Center for Special Separation Membrane, Nanjing Tech University, Nanjing 210009, PR China
[b] Chemical Engineering Department, Nanjing Polytechnic Institute, Nanjing 210048, PR China
[c] Centre for Advanced Separations Engineering and Department of Chemical Engineering, University of Bath, Claverton Down, Bath BA2 7AY, United Kingdom
[d] CAS Key Laboratory of Coastal Environmental Processes and Ecological Remediation, Research Center for Coastal Environmental Engineering and Technology of Shandong Province, Yantai Institute of Coastal Zone Research, Chinese Academy of Sciences, Yantai 264003, PR China

ARTICLE INFO

*Keywords:*
Formaldehyde degradation
Dynamic test
Indoor air filter
ZnO nanorods
Ag nanoparticles

ABSTRACT

It has been well recognized that there are a number of indoor contaminants including particulate matter, gaseous pollutants and microbials. The removal of indoor contaminants often requires multiple layers of various air filters. Herein, we report on a multifunctional air purifying filter produced by the hydrothermal growth of ZnO nanorod-wrapped PTFE nanofibers, constructed of nanostructured Ag deposited on the ZnO nanorods with a hierarchical structure for gas contaminant removal. Atomic layer deposition (ALD) was used to seed a layer of ZnO nanoseeds onto the PTFE fibrils which were then subjected to a hydrothermal reaction to form ZnO nanorods. Ag nanoparticels were subsequently assembled on the surface of the ZnO nanorods via a silver electroless deposition reaction. The resulting composite membrane exhibited an excellent dynamic antibacterial property of ~100% and a formaldehyde degradation rate of 60%. Compared with the pristine membrane, the gas permeation of the composite membrane increased from 227.26 $m^3\ m^{-2}\ h^{-1}\ kPa^{-1}$ to 275.36 $m^3\ m^{-2}\ h^{-1}\ kPa^{-1}$. The successful fabrication of this composite membrane with remarkable antibacterial and excellent formaldehyde degradation performance may provide a new route for the preparation of indoor air purification filters.

## 1. Introduction

A major component of modern-day indoor pollution is microscopic airborne solid material known as particulate matter (PM) or aerosols, which includes fine particles [1,2], bacteria [3–5], and hydrocarbons (toluene, xylene, formaldehyde and other organic components [6–9]). Among these, formaldehyde is one of the most prevalent pollutants in indoor air. These pollutants have serious environmental and health-related consequences that can cause adverse respiratory effects and even cancer [10]. Thus, it is of great interest to remove this PM, microbes, and formaldehyde from indoor air to help ameliorate these risks. However, conventional filters struggle to capture the fine dust with diameters lower than 0.3 μm, which is considered to be the most penetrating particle size (MPPS) [11]. Furthermore, bacteria contamination on the surface of commercial filters will inevitably lead to increased pressure drop across the filter and deterioration of the filter and its performance with the eventual release of microorganisms. In addition, conventional filters consist of multiple layers where each filter layer is able to filter only one particulate substance. They are incapable of removing formaldehyde from the air. Therefore, a multifunctional filter is needed for air contaminant removal with high PM capture efficiency and good antibacterial, and formaldehyde degradation performance.

The polytetrafluoroethylene (PTFE) membrane is one of the most commonly used filters for gas purification [12,13] thanks to its high gas flux, high chemical resistance and high water repellency [14–17]. In particular, the biaxial oriented PTFE membrane can be readily produced with good mechanical properties and a large amount of uniform micropores [12,18]. However, moist aerosols containing micro-dust and large amounts of microbes can cause pore blocking after filtration leading to a high pressure drop and low aerosol removal efficiency. Furthermore, the microbes accumulated on the filter will multiply rapidly, leading to poor air cleaning performance. Also, PTFE cannot be used for organic components degradation because PTFE lacks catalytic properties. Therefore, much effort is required to design advanced filters that combine the advantages of high particulate

* Corresponding author.

http://dx.doi.org/10.1016/j.memsci.2017.02.042
Received 24 November 2016; Received in revised form 14 February 2017; Accepted 27 February 2017
Available online 28 February 2017
0376-7388/

removal efficiency, low pressure drop, excellent bacteria inhibition, and good formaldehyde degradation capability.

Materials with antibacterial properties have been used as antimicrobial coatings on various surfaces, and have included organic antibacterial agents such as chitosan, capsaicin and pyridine-based polymers [19–21], and inorganic anti-bacterial agents such as $TiO_2$, ZnO, Cu, Ag, and so on [22–25]. Among these agents, ZnO is a multifunctional material with good catalytic, electrical, photochemical and optical properties [26–28]. Also, ZnO is a semiconductor with a large band gap that satisfies the band edge potential requirement. The polar structure of ZnO renders fast separation and transport of photogenerated electrons and holes [29]. On the other hand, nanosized silver is known for its antibacterial properties for a wide spectrum of pathogenic bacteria. Also, nano silver has a light-harvesting couple and catalytic functions that may further improve the photocatalytic performance for degradation of formaldehyde under light irradiation [30,31].

In our previous work, we have reported two kinds of ALD modified PTFE membrane. While the ZnO nanorods (ZnO-NRs) functionalized membrane [32] was used for air purification with excellent superfine dust rejection rate (99.9999%) at a comparative low pressure drop (40% lower than pristine membrane). The amphiphobic PTFE membrane [33], which is further modified by grafting a layer of low surface free energy monomer through glow discharge plasma, was used for oil aerosol control. The oil aerosol removal efficiency of this membrane is greater than 99.5%. In this work, we report on a multifunctional air purifying composite designed filter that consisted of a hierarchical Ag/ZnO-nanorod-wrapped PTFE nanofibrous membrane. ZnO nanoparticles (ZnO-NPs) were first seeded onto the PTFE fibers by atomic layer deposition followed by hydrothermal growth of ZnO nanoparticles to form a nanorod array around the fibers. Ag nanoparticles were subsequently deposited on the surfaces of ZnO-NRs. The gas flux, dynamic antibacterial performance and formaldehyde degradation efficiency of the new composite filters were evaluated.

## 2. Experiment section

### 2.1. Materials

Porous PTFE membranes with a mean pore diameter of 5 μm in the form of circular disc (diameter: 47 mm; thickness: 100 μm) were purchased from Sartorius (Goettingen, Germany) and used as received. The ALD reactants were diethyl zinc (DEZ, 98%, MO source center of Nanjing University) and deionized $H_2O$, which were used as the Zn and O precursors. High purity $N_2$ (99.99%) was used as the precursor carriers and purging gas. Zinc nitrate hydrate ($Zn(NO_3)_2{\cdot}6H_2O$) and hexamethylenetetramine (HMTA, $C_6H_{12}N_4$) were purchased from Shanghai Lingfeng Chemical Co. Silver nitrate ($AgNO_3$) was purchased from Chinese Medicine Group Chemical Reagent Co., Ltd. All chemical reagents were of analytical grade and were used as received without further purification.

### 2.2. Deposition of ZnO seeding layers (ZnO-NPs@PTFE)

The dried PTFE membranes were placed in the chamber of a commercialized ALD reactor (SavannahS100, Cambridge Nano-Tech) and dried at the operating temperature for 30 min under vacuum (~1 Torr). Both the DEZ and $H_2O$ were kept in the storage cylinders at room temperature. The generation of ZnO (in ALD process) is expressed by the equation:

$$Zn(C_2H_5)_2+H_2O = ZnO+2C_2H_6$$

In ALD, the substrate was exposed to alternating DEZ and $H_2O$ reactants and the resulting membrane was formed stepwise. The substrates were deposited for 150 cycles at 130 °C with a steady $N_2$ flow rate of 20 sccm. In a typical ALD cycle, the DEZ and water vapor were sequentially pulsed into the reactor for 0.03 s. Immediately after each pulse of precursors, the system was purged with nitrogen for 30 s to sweep off the excess precursor.

### 2.3. Hydrothermal growth of ZnO nanorods (ZnO-NRs@PTFE)

ZnO-ALD PTFE substrates were immersed in a 35 ml aqueous solution with equimolar (5 mM) zinc nitrate and HMTA in an autoclave (70 ml, Zhenghong, China). The reaction was conducted at 90 °C for 3 h. Subsequently, the sample was recovered and washed with deionized water before drying in air.

### 2.4. Deposition of Ag nanoparticles

Two ZnO-NRs@PTFE and ZnO-NPs@PTFE membranes with diameters of 47 mm and a thickness of 100 μm were prepared and no extra pretreatments were performed on the membrane prior to use. Ag nanoparticles were deposited on the ZnO nanorods by an electroless silver mirror reaction. Briefly, an ammonia solution (2.5–2.8 wt%) was first added dropwise to 5 ml of a silver nitrate solution (2 wt%) until the precipitate completely dissolved to form $[Ag(NH_3)_2]^+$. Then, 3 ml of a glucose solution (10 wt%) was added. The ZnO nanorods@PTFE membrane sample was immediately dipped into the silver mirror reaction bath for 10 min at 50 °C. This was followed by washing the membrane with distilled water and completely drying it in an oven at 120 °C for 30 min.

### 2.5. Static antibacterial test

The antimicrobial efficiency of the filter medium was examined against (*Escherichia coli* (ATCC11303), *E. coli*). *E. coli* was purchased from Shanghai Seebio Biotech, Inc. The antibacterial performances were determined as follows: the microbial species were grown in broth solutions (Luria–Bertani broth for *E. coli*) for 24 h at 37 °C. The bacteria were harvested by centrifugation, washed with phosphate buffered saline (PBS), and then resuspended in PBS to a density of colony forming units per milliliter (CFU $ml^{-1}$). 100 μl of the freshly prepared bacterial suspensions was placed onto the surfaces of filters samples ($3.0 \pm 0.1$ $cm^2$) under room lighting conditions. After 15 min, the sample was transferred to 10 ml of sterilized PBS and vortexed for 2 min to transfer the adherent bacteria into the PBS. The solution was then diluted serially and 100 μl of each diluent was placed onto agar plates (Luria–Bertani agar for *E. coli*). Colony forming units on the agar plates were counted under an optical microscope after incubation at 37 °C for 24 h. Each test was repeated for at least three times. The reported data were the average values of three parallel runs.

The antibacterial rate was determined by using the following formula:

$$\text{antibacterialrate}(\%) = \frac{A - B}{A} \times 100$$

where A (CFU) is the number of living bacterium in the control sample and B (CFU) is the number of living bacterium in the testing sample.

### 2.6. Dynamic antimicrobial test

The dynamic antibacterial test apparatus is shown in Fig. 1. The high concentration of bacterium liquid was first atomized using pure air through a collision nebulizer, then a sealed desiccator with full of silicone gel was used to dry the bacterium mixed air. The gas flow was controlled by a valve placed downstream from the gas cylinder. The gas velocity was maintained at 0.5, 1.5, 2.5, 3.5, and 4.5 cm/s. Two sampling ports were set before and after the membrane. The mixed air was run into a beaker containing a quantity of PBS, which had been sterilized before use. The sampling time was 15 min. To characterize the antibacterial performance, the bacterium solutions were sampled

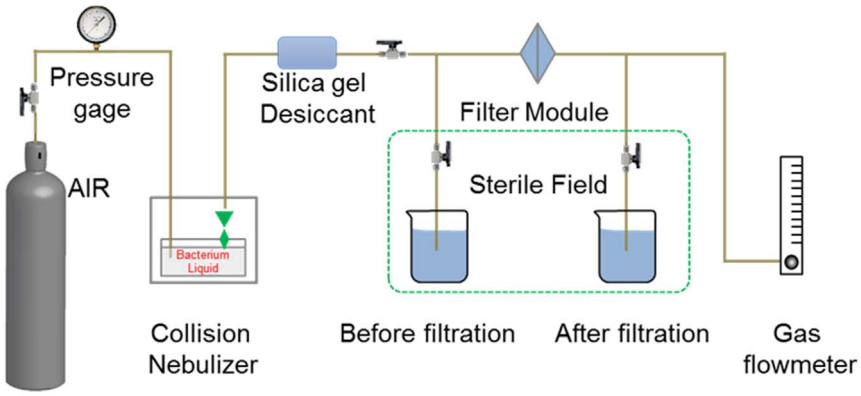


**Fig. 1.** Schematic diagram of the in-house dynamic antimicrobial test apparatus.

using a vis spectrophotometer (Orion Aquamate 7000, Thermo, US) at OD 633 nm after 4 h of culturing to detect the bacterial density of the collected bacteria solution. The bacterium solution and the bacterial counting method in this process were the same as those used in the static antimicrobial test. The antibacterial rate of dynamic test can be calculated by the formula:

$$\text{dynamic antibacterial rate}(\%) = \frac{c_0 - c}{c_0} \times 100$$

where $c_0$ (CFU/ml) is the bacterium concentration of the solution before filtration, and c (CFU/ml) is the bacterium concentration of the solution after filtration.

### 2.7. Formaldehyde degradation test

The formaldehyde degradation performance of the novel membranes was measured using an in-house test (Fig. S1), which was based on the dynamic antibacterial test apparatus. The flowing air was supplied by a gas cylinder. The inlet pressure of the membrane was 0.5–2.5kPa. The process was conducted at ambient temperature. The membrane test area was 7.07 $cm^2$ (φ=3 cm). The formaldehyde gas was generated from a formaldehyde solution with a concentration of 0.2%. The membrane module was placed on a clean lab bench with UV irradiation. To produce a good UV irradiation effect, the membrane module was made of quartz. To achieve higher loading of measurable formaldehyde, three slices of functionalized filters were clipped into a quartz module, with each filter divided by a slice of stainless steel wire mesh. The gas velocity was controlled at 0.5 cm/s using an intake valve. The formaldehyde concentration in the gas flow was measured using formaldehyde gas analyzer (Interscan 4160, US) before and after the membrane module.

## 3. Characterization

Surface morphology and microstructure of the sample membranes were analyzed using field emission scanning electron microscopy (FESEM, HitachiS-4800, Japan). Prior to SEM analysis, the samples were sputter-coated with a thin layer of a gold/palladium alloy. The samples for TEM (JEOL 3010, Japan) were initially scraped using a scraper, then they were ultrasonicated in 10 ml of ethyl alcohol for 3 h at 300 W at an ultrasound frequency of 40 kHz. The dispersed solution was then placed onto a copper wire mesh for TEM imaging. X-ray diffraction patterns of the samples were obtained using an X-ray diffractometer (XRD MiniFlex 600, Japan) with Cu Kα radiation (λ=0.154 nm) at a generator voltage of 40 kV and a generator current of 15 mA. The scanning speed was 10°/min and the step was 0.02°/min. The gas adsorption properties were carried out by N2 sorption at 77 K with a sorptometer (Micromeritics ASAP 2460) and the surface area was calculated by Brunauer–Emmett–Teller (BET) method. The pore size distribution of the membrane was determined using a pore-size distribution analyzer (PSDA-20, China) employing a bubble point method. The membrane was wetted before the test with an appropriate test fluid such as isopropyl alcohol. The inverse pressure - pore size relationship for a cylindrical pore can be expressed by the equation: ($D=4\gamma\cos\theta/\Delta P$) where D (μm) is pore diameter, γ (N/m) is the surface tension of wetting fluid, θ is the contact angle of wetting fluid on membrane surface and ΔP (Pa) is the pressure difference between gas and liquid. The gas flux was determined using a PSDA-20 by using cylinder nitrogen. The range of the operating pressure drop was from 0 to 10 kPa. The test area was 0.79 $cm^2$. The computer will show the gas flow at each pressure. Error bars in the plotted data represent the standard deviation of the gas flux derived from five individual measurements. The gas flux was calculated by the equation:

$$J = \frac{Q}{A}$$

Where J is the gas flux ($m^3/m^2$ h), Q is the gas flow rate detected by the instrument ($m^3/h$), A is the test area of the membrane ($0.79\times10^{-4}$ $m^2$).

Gas permeability was calculated by the following equation:

$$P = \frac{Q_p}{\Delta p \bullet A}$$

Where P is the gas permeability($m^3/m^2$ h kPa), $Q_p$ is the gas glow at a certain pressure($m^3/h$), Δp is the pressure difference of the membrane(kPa).

## 4. Results and discussion

### 4.1. Microstructure evolution and preparation schematic of the membrane

A schematic representation of the preparation and the morphology of the sample membranes at various stages of preparation are shown in Fig. 2(e). The preparation of the membrane was accomplished using three simple steps: 1) seeding a layer of nano-ZnO particles on the membrane surface by atomic layer deposition; 2) hydrothermal growth of ZnO-NRs on the seeding layer; 3) in situ formation of Ag-NPs on the surface of ZnO-NRs using an electroless silver reaction.

The PTFE membrane filters prepared by a stretching process were highly porous and exhibited a net-like structure comprised of interconnected and smooth nanofibrils. As shown in Fig. 2(a), the free spaces between the nanofibrils define the pores in the PTFE membrane filter. The ALD treatment process placed 3D ZnO-seeds wrapped around the PTFE nanofibrils (Fig. 2(b)), which enhanced the mechanical strength of the fibrils [33,34]. ZnO-NRs were grown on the seeded layer in a uniform array by hydrothermal growth. The SEM image (Fig. 2(c)) of the ZnO-NRs exhibited a hexagonal crystal growth (which confirmed the presence of the wurtzite crystal lattice of ZnO). Dense

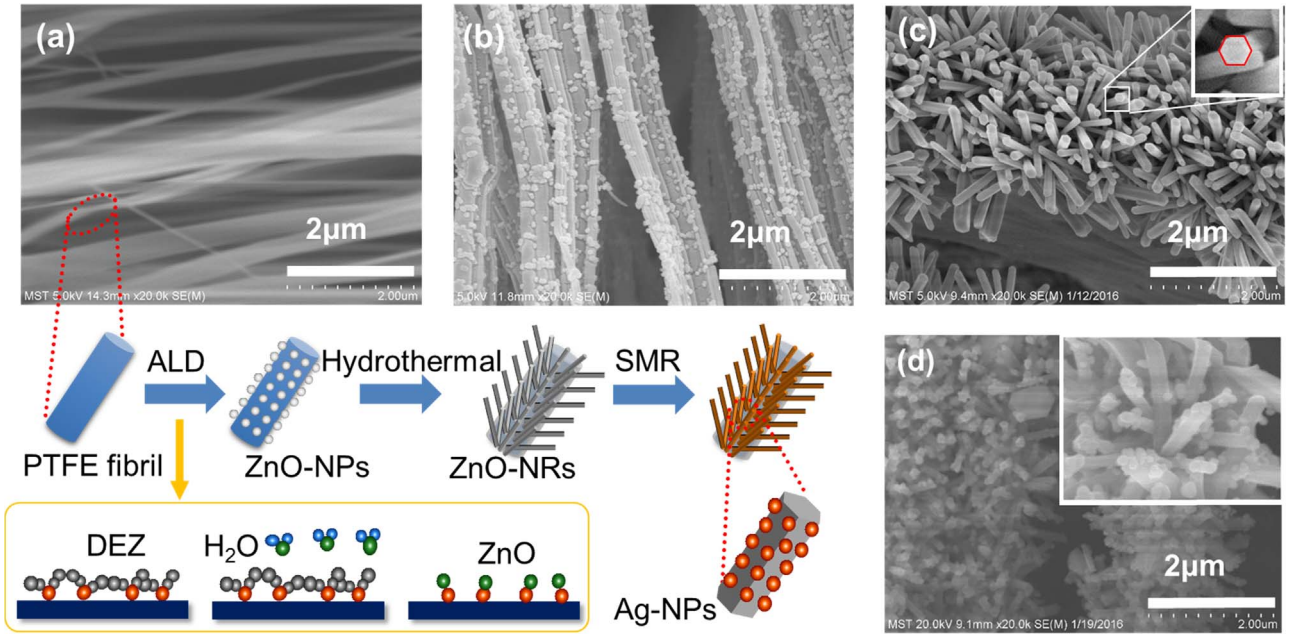


**Fig. 2.** Schematic of the preparation process of the Ag@ZnO-functionalized PTFE filters and the SEM images of the filters at different stages of production (a) Pristine PTFE, (b) ZnO-NPs@PTFE, (c) ZnO-NRs@PTFE, (d) Ag/ZnO-NRs@PTFE; inset is a high magnification micrograph of Ag/ZnO-NRs@PTFE; (e) Schematic of the preparation of Ag/ZnO-NRs@PTFE.

and uniform ZnO-NRs were grown vertically on the fibrils, which was conducive to enhancing the specific surface area of the membrane. The surface area of the filter increased to 7.4 $m^2 g^{-1}$ from 4.3 $m^2 g^{-1}$ in the case of the unmodified membrane. The ZnO-NRs formed a barrier that was 1–2 μm in length, which (Fig. S2) narrowed the space between the fibrils. This improved the dust collecting capability of the membrane [32], while the existence of a loose ZnO-NRs structure appeared to have no effect on the gas flux of this membrane. The ZnO-NRs functionalized PTFE membranes were then electrolessly coated with a layer of Ag nanoparticles. The Ag nanoparticles that adhered on the hexagonal ZnO-NRs had a diameter of 10–100 nm (Fig. 5(a)). The rod-like ZnO afforded a large number of combined reaction sites for the Ag-NPs.

### *4.2. Loading of Ag-NPs onto ZnO-NPs@PTFE and ZnO-NRs@PTFE membranes*

The ALD process resulted in the deposition of a layer of ZnO-NPs, with a loading of 15–20 wt% (Fig. S3). To calculate the loading of the ZnO-NRs and Ag-NPs, the ZnO-NPs@PTFE membrane was weighed before and after the hydrothermal growth process of the ZnO-NRs and the silver reaction process, respectively. Each sample was tested three times and the average results were obtained. Fig. 3(a) shows that the Ag-NPs adhered to the surface of the PTFE membrane and the particles had a diameter of 10–200 nm. The electroless silver reaction process resulted in small Ag particles that were somewhat monodispersed on the surface, but generation of larger particles was difficult to control. With the addition of $[Ag(NH_3)_2]^+$and glucose, additional silver ions were absorbed onto the surface of the ZnO-NPs@PTFE membrane and were reduced to metallic silver. These silver seeds then grew into Ag-NPs. For the ZnO-NRs@PTFE membrane, the large specific surface area offer more voids for the $[Ag(NH_3)_2]^+$ to react, so that the particle sizes of the Ag-NPs on ZnO-NRs@PTFE membrane were smaller than on the ZnO-NPs@PTFE membrane (Fig. 3(b)). The inset of Fig. 3(a) shows that the loading of the Ag-NPs (Ag-wt%/PTFE-wt%) was close to the loading of the ZnO-NPs (ZnO-wt%/PTFE-wt%) with values of 18.25% and 20.05%, respectively. However, the hydrothermal process improved the ZnO loading (from 20.05% to 88.57%). The weight of formed ZnO-NRs was close to that of the pristine membrane, indicating a large amount of ZnO-NRs were grown on the ZnO-NPs@PTFE

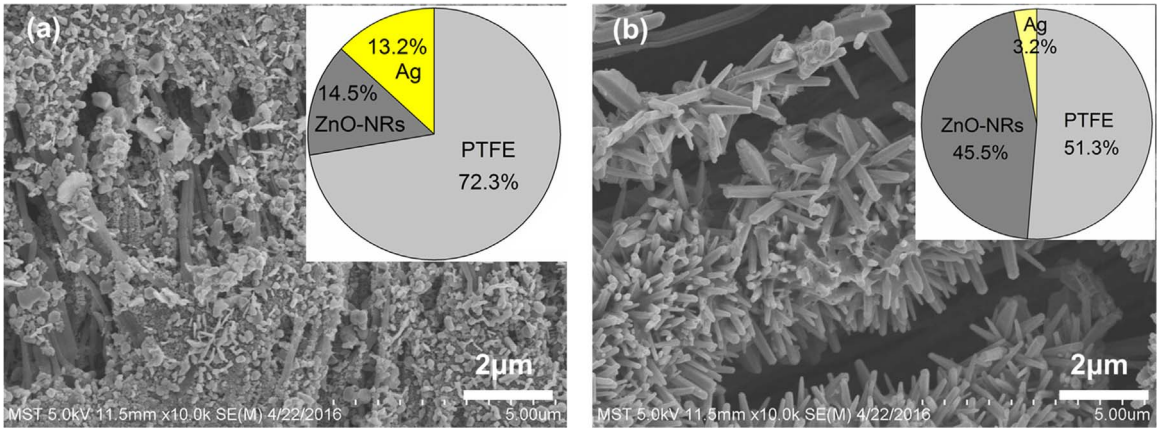


**Fig. 3.** SEM images of (a) Ag-NPs loaded on the ZnO-NPs@PTFE membrane; (b) Ag-NPs loaded on the ZnO-NRs@PTFE membrane; the insets are the loadings of Ag-NPs and ZnO-NRs for sample (a) and sample (b).

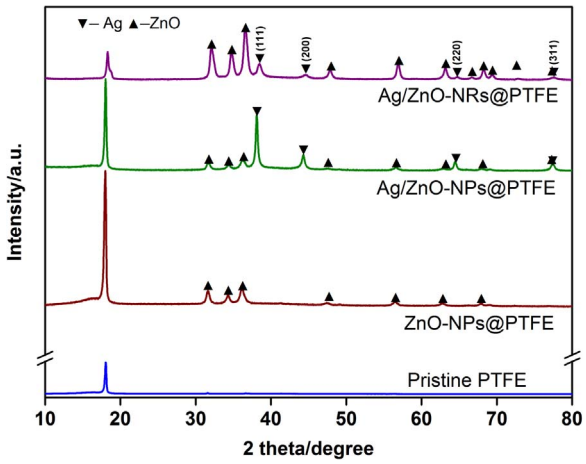


**Fig. 4.** XRD patterns of various membrane samples.

membrane after the hydrothermal process. The Ag-NPs loading was about 6.13% for Ag/ZnO-NRs@PTFE membrane, which was much lower than the Ag/ZnO-NPs@PTFE membrane.

### 4.3. Characterization of Ag and ZnO nanoparticles

The presence of Ag-NPs was confirmed by X-ray analysis of the membranes, as shown in Fig. 4. The peak centered at 18.06° was assigned to the crystalline PTFE. Three main peaks were observed after the ALD (ZnO-NPs) and hydrothermal growth (ZnO-NRs). These peaks were attributed to the (100), (002) and (101) planes of ZnO at 2θ of 32.08, 34.74 and 36.56° [35]. Using the Bragg equation, the interchain d-spacings were calculated to be 2.79, 2.58 and 2.46 Å,. From the XRD patterns of Ag/ZnO-NPs@PTFE and Ag/ZnO-NRs@PTFE, four distinct peaks were observed. Theses peaks appeared at 2θ values of 38.1, 44.3, 64.4, and 77.5°, which corresponded to the reflections of the (111), (200), (220) and (311) crystalline planes of silver [22]. The corresponding *d*-spacings were 2.36, 2.04, 1.45 and 1.23 Å, respectively. These values were consistent with the fringe separation as observed in the HRTEM results (Fig. 5). Moreover, the higher intensity of the peaks of Ag in the spectrum of the Ag/ZnO-NPs@PTFE suggested a higher loading of Ag-NPs. The TEM images (Fig. 5(a)) show that the Ag-NPs were dispersed with particle diameters ranging from 10 to 100 nm. Fig. 5(a, b) shows that the Ag-NPs were attached to the ZnO-NRs as a result of the electroless silver reaction. As shown in the HRTEM images (Fig. 5(c)), the clear lattice fringes with spacing of 0.26 nm corresponded to the spacing of the (002) planes of the ZnO. The lattice spacing of the crystalline phase was 0.20 nm (Fig. 5(d)), which corresponded to the (200) lattice planes of Ag [22,23]. The successful growth of Ag-NPs on ZnO-NRs is evident in Fig. 5(e), as indicated by the distinct interface between Ag-NPs and ZnO-NRs.

### 4.4. Gas permeation property of Ag/ZnO-NPs@PTFE and Ag/ZnO-NRs@PTFE membranes

Air permeability tests were conducted to evaluate the influence of the ZnO and Ag loadings on the gas flux of the pristine and modified PTFE filters. As shown in the insert in Fig. 6(a), the gas permeability of the pristine membrane was about 227.26 $m^3\ m^{-2}\ h^{-1}\ kPa^{-1}$. The ZnO-NPs@PTFE membrane exhibited an increase in the gas permeation rate of 21.16% to 275.36 $m^3\ m^{-2}\ h^{-1}\ kPa^{-1}$ as a result of a tiny-pore throat enlargement effect that resulted from the ALD process. During this process DEZ vapor, $H_2O$ vapor, and the sweep gas ($N_2$) were alternatively injected into the react chamber at a temperature of 130 °C. The comparatively cool sweep gas was blown over the hot membrane surface. This process is similar to the quenching treatment for steel production. The high temperature enlarged the tiny pores of the membrane. The carrying gas cooled the surface of the membrane, causing shrinkage of the membrane surface. The inner stress in the membrane resisted this behavior, so the pores enlarged by in the heated vapor sweep process were preserved. Meanwhile, the ALD process may lead to the membrane become fluffy, which is favorable for enlarger tiny pores of the membrane [36,37]. Fig. 6(b) shows that the pore size of pristine PTFE membrane was about 4.0 μm. After ALD treatment, the pore size of the membrane decreased to 3.0 μm. Even the tiny pores were enlarged by the ALD process, but the ZnO-NPs. wrapped on the fibers contributed to narrowing the space between the fibrils. It was evident that the formation of ZnO-NRs enlarged the diameter of the fibers containing rounded spines, which efficiently decreased the pore sizes in the filter (pore size 2.0 μm). Small grains of nano silver deposited on the ZnO-NRs cannot effectively increase the diameter of the fibers, so the pore size of Ag/ZnO-NRs@PTFE was only

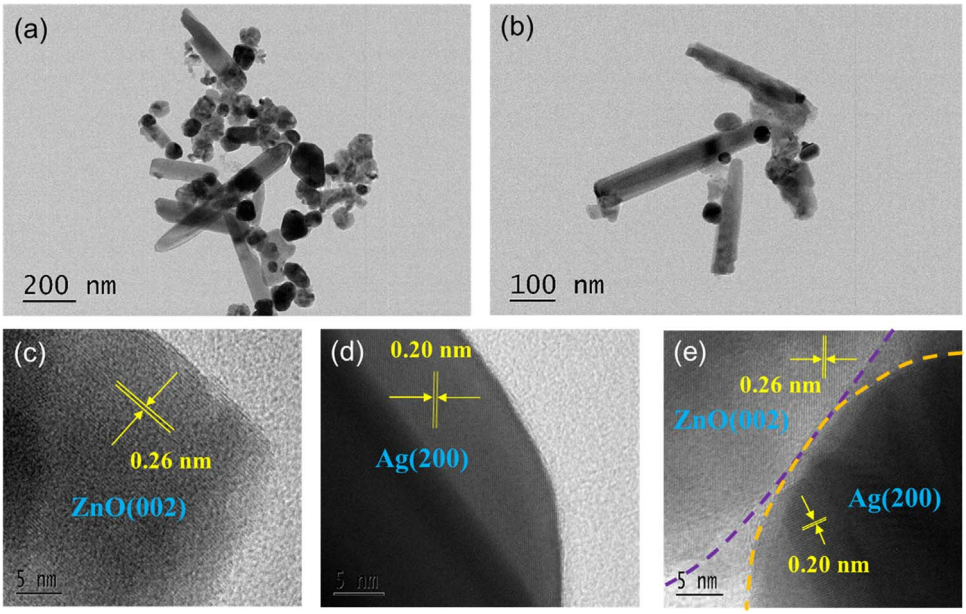


**Fig. 5.** (a), (b)TEM images of Ag@ZnO-NRs with different magnification; (c), (d) and (e). HRTEM images for various areas of the Ag@ZnO-NRs.

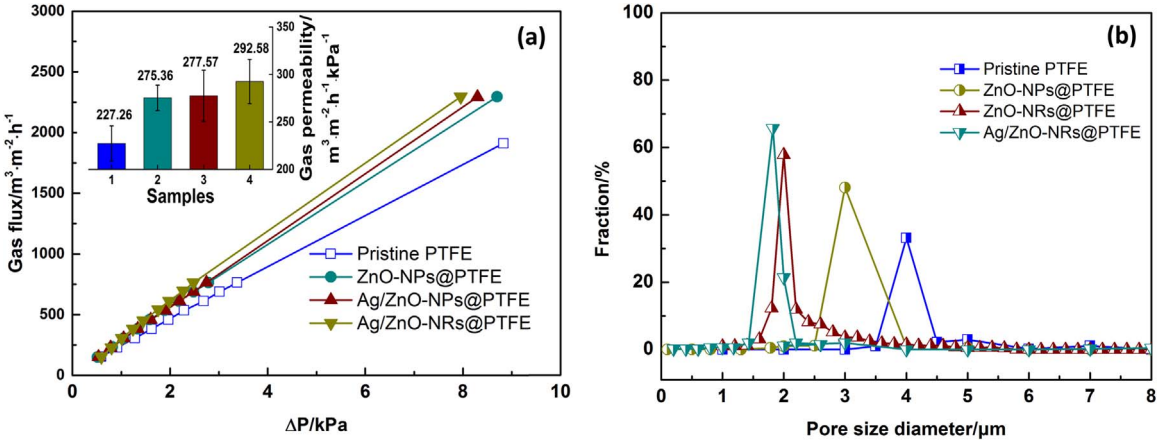


**Fig. 6.** (a) Gas flux of various membrane samples, inset shows the gas permeability of 1) pristine PTFE, 2) ZnO-NPs@PTFE, 3) Ag/ZnO-NPs@PTFE, 4) Ag/ZnO-NRs@PTFE, (b) Pore size distribution of functionalized membranes obtained at different production stages.

0.2 μm smaller than the ZnO-NRs@PTFE. The modification process narrowed the pore size distribution, while increasing the average pore size fraction of the membrane. Although there was a decrease in the average pore size of the ZnO-NRs@PTFE membrane and Ag/ZnO-NRs@PTFE membrane, the presence of loose ZnO-NRs and NPs had little effect on the membrane gas flux.

### 4.5. Antibacterial properties

Experimental results for the static antibacterial activity of the pristine membrane, and the ZnO-NRs@PTFE, Ag/ZnO-NPs@PTFE, and Ag/ZnO-NRs@PTFE membranes are presented in Fig. 7. Overnight incubation of the modified membrane (Fig. 7(c–e)) resulted in an approximately 99–100% reduction in the number of the bacterial colonies compared to control sample and untreated sample after 24 h. In the case of the Ag/ZnO-NPs@PTFE and Ag/ZnO-NRs@PTFE, a high reduction of bacteria occurred on both membranes. The reason for the antimicrobial properties of these membrane was attributed the presence of the ZnO-NRs and Ag-NPs, especially in the case of the Ag/ZnO-NRs@PTFE membrane. The release of silver ions from the functionalized filter had a significant antibacterial effect on *E. coli*. However, bacteria in the airflow are not always in contact with ZnO-NRs and Ag-NPs in a practical air purification process. Therefore, the dynamic antibacterial test is the better way to evaluate the antibacterial performance of the filter for air purification. The dynamic antibacterial results showed that the Ag/ZnO-NPs@PTFE and Ag/ZnO-NRs@PTFE filters had a good anti-bacterial property. A sample of a bacterial colony was grown on the agar plate (Fig. 8(a)), which was sampled from the beaker before filtration. The antibacterial performances of various samples after filtration are shown in Fig. 8(b–e). For the pristine PTFE membrane filtration test, a small fraction of bacteria was rejected while the rest of the material passed through the membrane (Fig. 8(b)). In the case of the Ag/ZnO-NPs@PTFE and Ag/ZnO-NRs@PTFE filters (Fig. 8(d, e)), scarcely any bacteria was observed on the agar plate, which demonstrated the excellent antibacterial performance of the nano-Ag and nano-ZnO modified filters with an antibacterial rate close to 99–100%. The bactericidal effect of the Ag and ZnO-NPs in the filters can be explained by their nano-scale size and exceptional properties. Their nanoparticles exhibited more pronounced bacterial effects towards a broad range of microorganisms. This small particle size allowed for better penetration and interaction with the bacteria, disrupting the cell membrane and hence their effectiveness as bactericidal materials was increased compared to the membrane that lacked nanoparticle modified materials [38]. Further, ZnO-NRs arrays wrapped around the fibrils narrowed the space between each fibril, resulting in a sieving filtration. The homogeneous formation and intensive distribution of small Ag-NPs on ZnO-NRs arrays offered more chances for the bacterial cells to contact with the Ag-NPs directly. The release of both $Ag^{+}$ and $Zn^{2+}$ from the nanomaterials contributed to the antimicrobial activity of the membrane [39,40]. Fig. 9 shows that the Ag/ZnO-NRs@PTFE or ZnO-NRs@PTFE filters could effectively suppress the bacterial growth compared to the sample without the particulate functionalization. Experimental results revealed that both modified filters had good antibacterial performance (antibacterial rate=99.5%) with a gas velocity below 2.5 cm/s. At this flow rate, bacteria can be easily captured and sterilized by the filter with a comparative long contact time. When the gas velocity was higher than 2.5 cm/s, the comparative high gas velocity will cause most of the bacteria to pass through the filter along with the airstream. Also, the contact time between the bacteria and the filter is too short to allow the membrane to kill the bacteria efficiently. Nevertheless the Ag/ZnO-NRs@PTFE filter showed better antibacterial performance (≈98%) than the membrane without Ag-NPs (≈80%) when the gas velocity was greater than 2.5 cm/s, because the antibacterial performance of $Ag^{+}$ was better than $Zn^{+}$. Besides, antibacterial materials prevent the reproduction of microbials on the membrane surface which is significant for the filter to maintain a steady operating pressure drop.

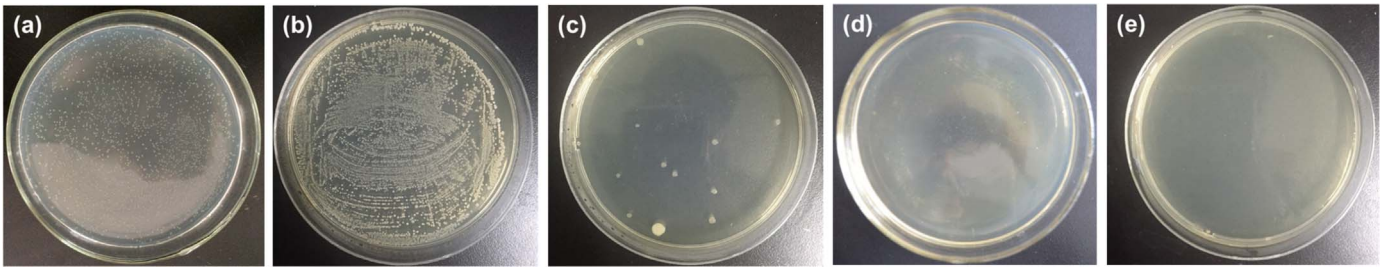


**Fig. 7.** Static antibacterial activity of various samples against *E. coli* (ATCC11303), (a) control sample. (b)pristine membrane, (c) ZnO-NRs@PTFE. (d)Ag/ZnO-NPs@PTFE. (e) Ag/ZnO-NRs@PTFE.

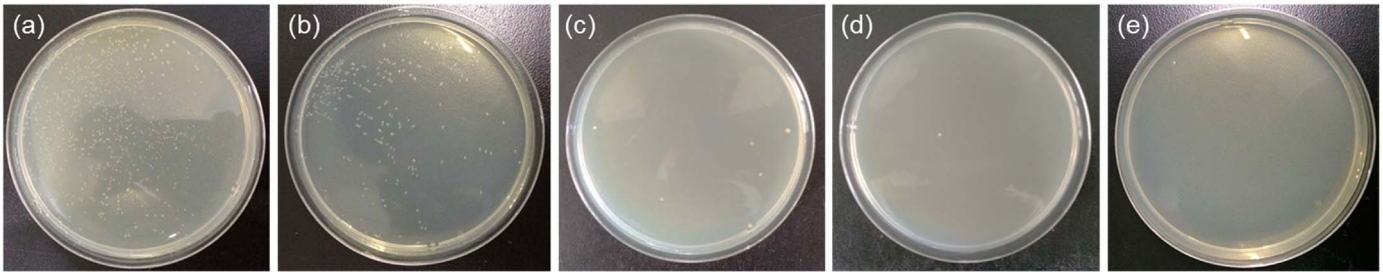


**Fig. 8.** Dynamic antibacterial test. (a)Antibacterial activity before filtration. Antibacterial activity of each samples after filtration (b)pristine membrane, (c) ZnO-NPs@PTFE, (d) Ag/ZnO-NPs@PTFE, (e) Ag/ZnO-NRs@PTFE.

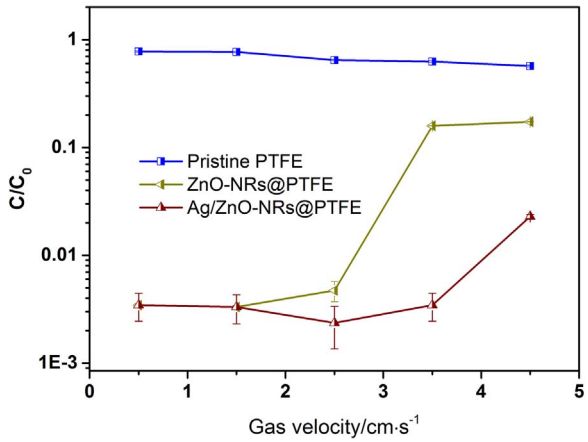


**Fig. 9.** Dynamic antibacterial performances of pristine PTFE, ZnO-NRs@PTFE, and Ag/ZnO-NRs@PTFE filter at different gas velocity.

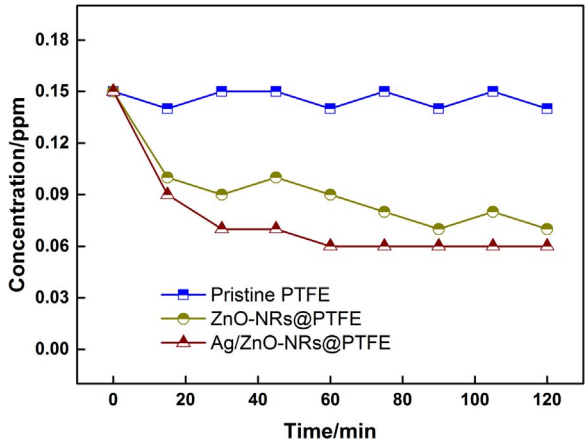


**Fig. 10.** Dynamic photocatalytic formaldehyde performance of various membrane samples, along with the filtration time from 0 to 120 min at the gas velocity of 0.5 cm/s.

### 4.6. Photocatalytic formaldehyde characterization

The photocatalytic activities of the functionalized filters were evaluated for the decomposition of formaldehyde. As shown in Fig. 10, for the ZnO-NRs@PTFE and Ag/ZnO-NRs@PTFE membranes the concentration of formaldehyde in the outlet stream decreased with exposure to UV irradiation. The formaldehyde removal ratios of the ZnO-NRs@PTFE filter was about 53%, while pristine PTFE filter produced no formaldehyde degradation. The sample Ag/ZnO-NRs@PTFE showed better photocatalytic activity with a formaldehyde removal ratio of about 60%, which was greater than the membrane without the Ag-NPs. Both the modified filters showed a steady state conversion of formaldehyde for 2 h. The presence of ZnO-NRs significantly affected the photocatalytic activity of the functionalized filter. Moreover, it was found that the formaldehyde removal efficiencies of the Ag/ZnO-NRs@PTFE filter increased by about 7% compared to the membrane without Ag-NPs. The outstanding UV photocatalytic performance of the functionalized filter was attributed to the presence of the nano-sized ZnO and Ag-NPs on the filter fibrils. The ZnO NRs wrapped around the fibrils enlarged the specific surface area for a more efficient electroless deposition of silver on the membrane which produced nanoparticles with a well-defined structure and excellent spatial distribution. The high activity of these increased the effectiveness of the photocatalytic efficiency of the membrane by the interaction of the nano silver particles with the zinc oxide [41]. The metal nanoparticles were believed to have acted as electron trapping sites which produced improved electron-hole separation during the photocatalytic decomposition reaction [27,30]. The formaldehyde photooxidation proceeded as shown in the following Eq. (1).

$$Zn^{2+}\text{-}O^{2-} \xrightarrow{h\nu} Zn^{+}\text{-}O^{-} \xrightarrow{HCHO+O_2} Zn^{2+}\text{-}O^{2-} \quad (H_2O+CO_2) \qquad (1)$$

First, when ZnO was illuminated by UV irradiation, surface electron ($Zn^+$) and hole ($O^-$) centers are generated. Then, HCHO reacts with $O_2$ to form $H_2O$ and $CO_2$ ($HCHO + O_2 \rightarrow CO_2 + H_2O$).

## 5. Conclusions

In this study, a three-step approach was initiated to produce Ag deposited ZnO-NRs-wrapped nanofibril PTFE filter membranes that resulted in a hierarchical structure with a number of active sites for multiple applications. The growth of ZnO-NRs wrapped around the fibrils enlarged the specific surface area of the membrane and narrowed the space between each fibril. Also, both ZnO and Ag contributed to the antibacterial performance of the filter, where a dynamic antibacterial ratio of 99.9% was achieved. The nanostructures of the ZnO and Ag particles attached to the membrane significantly enhanced its photocatalytic activity for the degradation of formaldehyde. When exposed to UV light, a formaldehyde removal efficiency of 60% was achieved by the modified membranes. The successful fabrication of this composite membrane with remarkable antibacterial and excellent formaldehyde degradation performance provides a new route for the preparation of indoor air purification hybrid filters.

## Acknowledgements

Financial support was provided by the National Natural Science Foundation of China (21276124), The National Key R&D Program (2016YFC0204000), Jiangsu Province Scientific Supporting Project (BE2014717 and BE2015023), and Key Program of Nanjing Polytechnic Institute (NHKY-2016-01).

## Appendix A. Supporting information

Supplementary data associated with this article can be found in the online version at doi:10.1016/j.memsci.2017.02.042.

## References


[1] C. Liu, P.C. Hsu, H.W. Lee, M. Ye, G. Zheng, N. Liu, W. Li, Y. Cui, Transparent air filter for high-efficiency PM2.5 capture, Nat. Commun. 6 (2015) 6205.
[2] T. Fedel, Air filtration: evaluating filtration efficiency, Filtr. + Sep. 49 (2012) 37–39.
[3] J.H. Jung, G.B. Hwang, J.E. Lee, G.N. Bae, Preparation of airborne Ag/CNT hybrid nanoparticles using an aerosol process and their application to antimicrobial air filtration, Langmuir: ACS J. Surf. Colloids 27 (2011) 10256–10264.
[4] Z. Wang, J.S. Zhang, Characterization and performance evaluation of a full-scale activated carbon-based dynamic botanical air filtration system for improving indoor air quality, Build. Environ. 46 (2011) 758–768.
[5] H. Wu, Z. Yin, Y. Quan, Y. Fang, C. Yin, Removal of methyl acrylate by ceramic-packed biotrickling filter and their response to bacterial community, Bioresour. Technol. 209 (2016) 237–245.
[6] T. Salthammer, S. Mentese, R. Marutzky, Formaldehyde in the indoor environment, Chem. Rev. 110 (2010) 2536–2572.
[7] J.M. Daisey, W.J. Angell, M.G. Apte, Indoor air quality, ventilation and health symptoms in schools_an analysis of existing information, Indoor Air 13 (2003) 53–64.
[8] K. Everaert, J. Baeyens, Catalytic combustion of volatile organic compounds, J. Hazard. Mater. 109 (2004) 113–139.
[9] F.I. Khan, A.K. Ghoshal, Removal of volatile organic compounds from polluted air, J. Loss Prev. Process Ind. 13 (2000) 527–545.
[10] B. Moser, F. Bodrogi, G. Eibl, M. Lechner, J. Rieder, P. Lirk, Mass spectrometric profile of exhaled breath–field study by PTR-MS, Respir. Physiol. Neurobiol. 145 (2005) 295–300.
[11] P. Li, C. Wang, Y. Zhang, F. Wei, Air filtration in the free molecular flow regime: a review of high-efficiency particulate air filters based on carbon nanotubes, Small 10 (2014) 4543–4561.
[12] Y. Guo, J. Chen, X. Hao, J. Zhang, X. Feng, H. Zhang, A novel process for preparing expanded polytetrafluoroethylene(ePTFE) micro-porous membrane through ePTFE/ePTFE co-stretching technique, J. Membr. Sci. 42 (2006) 2081–2085.
[13] R.R. Larson, M.B. Khazaeli, H.K. Dillon, A new monitoring method using solid sorbent media for evaluation of airborne cyclophosphamide and other antineoplastic agents, Appl. Occup. Environ. Hyg. 18 (2003) 120–131.
[14] P. Glaris, J.-F. Coulon, M. Dorget, F. Poncin-Epaillard, Thermal annealing as a new simple method for PTFE texturing, Polymer 54 (2013) 5858–5864.
[15] A. Ranjbarzadeh-Dibazar, P. Shokrollahi, J. Barzin, A. Rahimi, Lubricant facilitated thermo-mechanical stretching of PTFE and morphology of the resulting membranes, J. Membr. Sci. 470 (2014) 458–469.
[16] Q. Xu, Y. Yang, J. Yang, X. Wang, Z. Wang, Y. Wang, Plasma activation of porous polytetrafluoroethylene membranes for superior hydrophilicity and separation performances via atomic layer deposition of TiO2, J. Membr. Sci. 443 (2013) 62–68.
[17] S. Paria, N.R. Biswal, R.G. Chaudhuri, Surface tension, adsorption, and wetting behaviors of natural surfactants on a PTFE surface, AIChE J. 61 (2015) 655–663.
[18] K. Kurumada, T. Kitamura, N. Fukumoto, M. Oshima, M. Tanigaki, S. Kanazawa, Structure generation in PTFE porous membranes induced by the uniaxial and biaxial stretching operations, J. Membr. Sci. 149 (1998) 51–57.
[19] M. Cai, J. Chen, M. Taha, Synthesis, characterization, and antibacterial activity of yttrium(III) complexes with 2,6-pyridinedicarboxylate and pyridine, J. Coord. Chem. 64 (2011) 314–322.
[20] L. Fan, L. Yu, Y. Xu, C. Yi, J. Cai, M. Li, J. Huang, The novel alginate/N-succinyl-chitosan antibacterial blend fibers, J. Appl. Polym. Sci. (2010) NA-NA.
[21] X. Liu, T. Lin, B. Peng, X. Wang, Antibacterial activity of capsaicin-coated wool fabric, Text. Res. J. 82 (2011) 584–590.
[22] S.-C. Huang, K.M. Hsieh, T.W. Chang, Y.C. Chen, C.-T. Ricky Yu, T.-C. Lu, C.F. Lin, T.-Y. Yu, T.-T. Wang, H. Chen, ZnO nanoflakes on silver wires with antibacterial effects, Ceram. Int. 42 (2016) 7848–7851.
[23] J. Hu, Z. Zhong, F. Zhang, W. Xing, Z.-X. Low, Y. Fan, Coating of ZnO nanoparticles onto the inner pore channel surface of SiC foam to fabricate a novel antibacterial air filter material, Ceram. Int. 41 (2015) 7080–7090.
[24] N. Gao, Y. Chen, J. Jiang, Ag@Fe2O3-GO nanocomposites prepared by a phase transfer method with long-term antibacterial property, ACS Appl. Mater. Interfaces 5 (2013) 11307–11314.
[25] F. Fu, L. Li, L. Liu, J. Cai, Y. Zhang, J. Zhou, L. Zhang, Construction of cellulose based ZnO nanocomposite films with antibacterial properties through one-step coagulation, ACS Appl. Mater. Interfaces 7 (2015) 2597–2606.
[26] A. Pal, T.K. Dey, A. Singhal, R.C. Bindal, P.K. Tewari, Nano-ZnO impregnated inorganic–polymer hybrid thinfilm nanocomposite nanofiltration membranes: an investigation of variation in structure, morphology and transport properties, RSC Adv. 5 (2015) 34134–34151.
[27] S.G. Kumar, K.S.R.K. Rao, Zinc oxide based photocatalysis: tailoring surface-bulk structure and related interfacial charge carrier dynamics for better environmental applications, RSC Adv. 5 (2015) 3306–3351.
[28] R. Zou, G. He, K. Xu, Q. Liu, Z. Zhang, J. Hu, ZnO nanorods on reduced graphene sheets with excellent field emission, gas sensor and photocatalytic properties, J. Mater. Chem. A 1 (2013) 8445.
[29] L. Jiang, Y. Zhang, Y. Qiu, Z. Yi, Improved photocatalytic activity by utilizing the internal electric field of polar semiconductors: a case study of self-assembled NaNbO3oriented nanostructures, RSC Adv. 4 (2014) 3165–3170.
[30] J. Gamage McEvoy, Z. Zhang, Synthesis and characterization of Ag/AgBr–activated carbon composites for visible light induced photocatalytic detoxification and disinfection, J. Photochem. Photobiol. A: Chem. 321 (2016) 161–170.
[31] X. Chen, Y. Li, X. Pan, D. Cortie, X. Huang, Z. Yi, Photocatalytic oxidation of methane over silver decorated zinc oxide nanocatalysts, Nat. Commun. 7 (2016) 12273.
[32] Z. Zhong, Z. Xu, T. Sheng, J. Yao, W. Xing, Y. Wang, Unusual air filters with ultrahigh efficiency and antibacterial functionality enabled by ZnO nanorods, ACS Appl. Mater. Interfaces 7 (2015) 21538–21544.
[33] S. Feng, Z. Zhong, F. Zhang, Y. Wang, W. Xing, Amphiphobic polytetrafluoroethylene membranes for efficient organic aerosol removal, ACS Appl. Mater. Interfaces 8 (2016) 8773–8781.
[34] S.-M. Lee, V. Ischenko, E. Pippel, A. Masic, O. Moutanabbir, P. Fratzl, M. Knez, An alternative route towards metal-polymer hybrid materials prepared by vapor-phase processing, Adv. Funct. Mater. 21 (2011) 3047–3055.
[35] A. Gupta, K. Mondal, A. Sharma, S. Bhattacharya, Superhydrophobic polymethylsilsesquioxane pinned one dimensional ZnO nanostructures for water remediation through photo-catalysis, RSC Adv. 5 (2015) 45897–45907.
[36] A.H. Brozena, C.J. Oldham, G.N. Parsons, Atomic layer deposition on polymer fibers and fabrics for multifunctional and electronic textiles, J. Vac. Sci. Technol. A: Vac. Surf. Films 34 (2016) 010801.
[37] W.J. Sweet 3rd, C.J. Oldham, G.N. Parsons, Atomic layer deposition of metal oxide patterns on nonwoven fiber mats using localized physical compression, ACS Appl. Mater. Interfaces 6 (2014) 9280–9289.
[38] S.C. Motshekga, S.S. Ray, M.S. Onyango, M.N. Momba, Microwave-assisted synthesis, characterization and antibacterial activity of Ag/ZnO nanoparticles supported bentonite clay, J. Hazard. Mater. 262 (2013) 439–446.
[39] K. Ravichandran, N. Chidhambaram, S. Gobalakrishnan, Copper and Graphene activated ZnO nanopowders for enhanced photocatalytic and antibacterial activities, J. Phys. Chem. Solids 93 (2016) 82–90.
[40] Y. Chen, W.H. Tse, L. Chen, J. Zhang, Ag nanoparticles-decorated ZnO nanorod array on a mechanical flexible substrate with enhanced optical and antimicrobial properties, Nanoscale Res. Lett. 10 (2015) 106.
[41] L. Xiong, Q. Zhong, Q. Chen, S. Zhang, TiO2 nanotube-supported V2O5 catalysts for selective NO reduction by NH3, Korean J. Chem. Eng. 30 (2013) 836–841.